

A three-dimensional vertex dynamics cell model of space-filling polyhedra simulating cell behavior in a cell aggregate

Hisao Honda^{a,b,*}, Masaharu Tanemura^b, Tatsuzo Nagai^c

^aHyogo University, Kakogawa, Hyogo 675-0195, Japan

^bInstitute of Statistical Mathematics, Minami-Azabu 4-6-7, Minato-ku, Tokyo 106-8569, Japan

^cPhysics Department, Kyushu Kyoritsu University, Kitakyushu 807-8585, Japan

Received 12 March 2003; received in revised form 5 October 2003; accepted 6 October 2003

Abstract

We developed a three-dimensional (3D) cell model of a multicellular aggregate consisting of several polyhedral cells to investigate the deformation and rearrangement of cells under the influence of external forces. The polyhedral cells fill the space in the aggregate without gaps or overlaps, consist of contracting interfaces and maintain their volumes. The interfaces and volumes were expressed by 3D vertex coordinates. Vertex movements obey equations of motion that rearrange the cells to minimize total free energy, and undergo an elementary process that exchanges vertex pair connections when vertices approach each other. The total free energy includes the interface energy of cells and the compression or expansion energy of cells. Computer simulations provided the following results: An aggregate of cells becomes spherical to minimize individual cell surface areas; Polygonal interfaces of cells remain flat; Cells within the 3D cell aggregate can move and rearrange despite the absence of free space. We examined cell rearrangement to elucidate the viscoelastic properties of the aggregate, e.g. when an external force flattens a cell aggregate (e.g. under centrifugation) its component cells quickly flatten. Under a continuous external force, the cells slowly rearrange to recover their original shape although the cell aggregate remains flat. The deformation and rearrangement of individual cells is a two-step process with a time lag. Our results showed that morphological and viscoelastic properties of the cell aggregate with long relaxation time are based on component cells where minimization of interfacial energy of cells provides a motive force for cell movement.

© 2003 Elsevier Ltd. All rights reserved.

Keywords: 3D vertex dynamics; Interface energy; Polyhedral cell model; Vertex reconnection; Viscoelastic cell aggregate

1. Introduction

Tissues consist of cells that reflect their properties. Conversely, properties of the tissue influence the component cells. For example, an assembly of cells forms a spherical cell aggregate. When an applied force flattens the cell aggregate, the component cells also flatten initially, but then rearrange to recover their original shape (Phillips et al., 1977; Phillips and Steinberg, 1978; Phillips and Davis, 1978). Furthermore, when the component cells of a tissue exhibit apical-basal polarity, the cell aggregate may begin epithelial morphogenesis, e.g. forming follicles, tubes, branching structures, etc. The epithelium maintains its polarity and constrains its component cells to exhibit polarity in

the tissue. To investigate the relation between a tissue and its component cells, we need a cell model that faithfully simulates actual cell shapes and behaviors, and could be applied to various types of tissues.

Geometrical cell shape in a tissue has been investigated since Lewis (1923, 1928, 1931, 1943, etc.) modeled using computer simulations (Honda, 1978; Honda and Eguchi, 1980), and reviewed and discussed (Dormer, 1980; Honda, 1983; Weaire and Rivier, 1984; Dubertret and Rivier, 2000). At present, several cell models of cell geometry have been described using polygons or polyhedra to investigate cell aggregates or tissues. These models fall into four main groups, topology dynamics, center dynamics, boundary dynamics and vertex dynamics models. Topology dynamics cell models treat the distribution of topological cell shapes in a steady state including cell division and detachment (Dubertret and Rivier, 1997, 2000). Center dynamics cell models assume that Voronoi (or Dirichlet) domains can approximate

*Corresponding author. Hyogo University, Kakogawa, Hyogo 675-0195, Japan. Tel.: +81-794-27-5111; fax: +81-794-27-5112.

E-mail address: hihonda@hyogo-dai.ac.jp (H. Honda).

a polygonal cell pattern, which is described by the positions of the cell centers (Honda, 1978). Such a model was used to describe cell arrangement in the epidermis (Honda et al., 1979, 1996; Honda and Oshibe, 1984), cell division (Honda et al., 1984) and intermingling of two types of cells (Honda et al., 1990, 2000; Tanemura et al., 1991). Bodenstein (1986) developed a disk cell model to simulate tissue growth and cell patterning. Graner and Sawada (1993) proposed a Hamiltonian formalism using a center dynamics model to investigate cell patterning due to cell rearrangement. Rivier and Dubertret (1995) with correction by Rivier and Dubertret (1998) modified the Voronoi construction to include cell division and detachment in the basal layer of the epidermis. Clem et al. (1997) used a three-dimensional (3D) spherical cell model to simulate epithelial tissue renewal. Bretschneider et al. (1999) used a spherical cell model to simulate cell movement under chemotaxis in a cell aggregate of *Dictyostelium discoideum*. Drasdo and Forgacs (2000) simulated cell cleavage, blastulation and gastrulation based on the interaction energy in the contact region between two neighboring cells. Palsson developed a 3D cell model consisting of deformable viscoelastic ellipsoids to investigate collective cell movement, including cell sorting and morphogenesis in *Dictyostelium* (Palsson and Othmer, 2000; Palsson, 2001). Meineke et al. (2001) used a center dynamics model, including cell division, to simulate cell movements in the intestinal crypt. The third type of model uses a polygonal cellular pattern described by vertices at which three edges meet in 2D. Cell patterns described by vertices can change flexibly and the polygons can mimic real cells closely. For example, polygonal cell patterns with vertices that minimize the cell boundary rearrange to produce characteristic patterns that include many hexagonal or square cells (Honda and Eguchi, 1980; Honda et al., 1982, 1986; Stein and Gordon, 1982; Honda, 1983). A vertex dynamics model was used to simulate morphogenesis in *Fundulus* epiboly (Weliky and Oster, 1990) and notochord development in the African frog *Xenopus laevis* (Weliky et al., 1991). Another vertex dynamics model was developed to describe coarsening of cellular structures in soap froths and polycrystalline materials by deriving equations of motion for vertices and introducing elementary processes of vertex pair connections (Nagai et al., 1988, 1990; Kawasaki et al., 1989; Fuchizaki et al., 1995). It was modified to treat biological cells by including an additional potential term which restricts the motion of vertices (Nagai and Honda, 2001). Vertex dynamics models are a class of finite element model, e.g. see the investigations of cell rearrangement of two types of cells in a cell aggregate (Chen and Brodland, 2000; Brodland and Chen, 2000a, b). The fourth type of model is a boundary dynamics cell model designed to describe cell patterns by

the shape of their boundaries. One of such models is an extended version of the Potts model involving Monte Carlo dynamics. It was obtained by introducing a cell size constraint and different surface energies between different cell types into the Potts model for a biological cell aggregate (Graner and Glazier, 1992; Glazier and Graner, 1993; Mombach et al., 1995; Savill and Hogeweg, 1997; Marée and Hogeweg, 2001, 2002). It allowed comprehensive study of rearrangements of two types of cells in cell aggregates (Glazier and Graner, 1993). Another boundary dynamics model was given by Discher et al. (1998) who modeled the cell surface of a single cell using geometrical and elastic chain networks.

To investigate the cell shape, deformation and rearrangement of cells in 3D multicellular aggregates, the present paper extends our 2D vertex dynamics model for biological cells (Nagai and Honda, 2001) to a 3D version, which directly provides the vertex positions of cells and the shapes of cell surfaces in a cell aggregate. The 3D vertex dynamics model was confirmed to simulate behaviors of cells minimizing cell interface areas. A cell aggregate, when subjected to mechanical deformation, relaxes as elastic materials on short time-scale and as viscous liquids on long time-scales (Forgacs et al., 1998). The 3D vertex dynamics model provides an additional insight into the role of cell mechanical properties in the behavior of viscoelastic tissues.

The present paper is written for biologists and general physicists including theoreticians and computer scientists. Some parts are more technical for biologists and experimental physicists. We indicate these parts here. The paper is constructed so that, without understanding these technical parts precisely, the readers could grasp the biological aspects of the paper. All parts in Section 2. Models and Computer Simulation; Section 4.2. The polyhedral cell models in a 3D aggregate; Section 4.3. Minimization of the potential U and the role of the elementary process of reconnection; Section 4.4. Viscoelastic cell aggregates in Discussion; and Appendixes A–D.

2. Model and computer simulation

2.1. Cells and vertices

We consider a tissue consisting of many cells to be a 3D space tessellation, which consists of convex polyhedra without gaps or overlaps. When we consider topologically stable random cellular structures, a vertex in 3D space generally connects to four neighboring vertices by four edges (Weaire and Rivier, 1984). In a tessellation pattern, four neighboring cells determine a vertex at which four edges meet (Fig. 1a). We do not

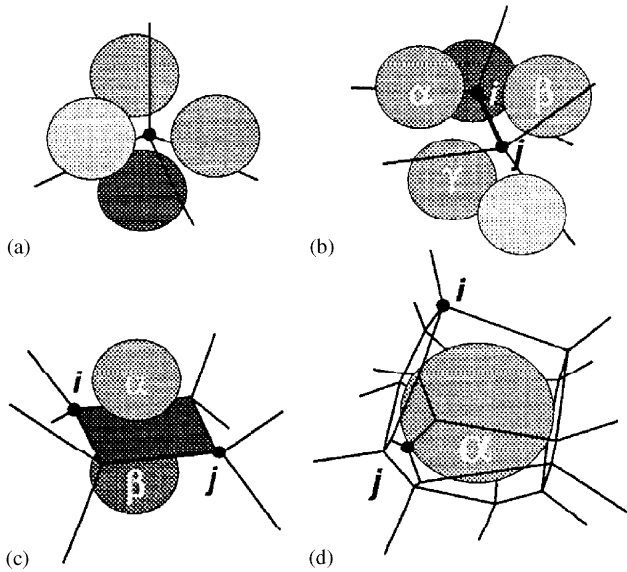


Fig. 1. Configuration of cells determines vertices, edges, interfaces and polyhedra (spheres represent cell centers). (a) Four cells determine one vertex at which four edges meet. (b) Three cells (α, β, γ) determine one edge connecting two vertices i and j . (c) Two cells (α, β) determine an interface involving two vertices i and j . (d) A cell (α) determines a polyhedron involving two vertices i and j . See Appendix A.

consider, in this paper, tessellations where more than four edges meet at a vertex. An assembly of vertices connecting to four neighboring vertices can form various networks, including the diamond structure and its variants (Wooten et al. 1985; Wooten, 2002). Among these, however, we consider only a 3D space tessellation pattern, which we consider to consist of faces, rather than edges, because we treat a cell aggregate as consisting of cell membranes, not of atoms and bonds as in amorphous materials.

We treat interfaces between neighboring cells and volumes of polyhedral cells in a 3D cell model. To present interfaces and volumes, we have to use vertices. Spatial relationships between cells and vertices in a 3D space tessellation are as follows: Three neighboring cells (α, β and γ) determine an edge. The edge is an intersection of three boundary surfaces (Fig. 1b). Each boundary surface is determined by a pair of cells. In Fig. 1b, cells α and β determine a boundary surface. Cells β and γ determine another boundary surface, and cells γ and α determine another boundary surface. These three surface boundaries determine the edge ij . Two neighboring cells (α and β) in 3D space determine a boundary surface between them (Fig. 1c). A cell corresponds to a polyhedron constructed of polygons (Fig. 1d). The tessellation pattern of a cell aggregate is completely defined by the coordinates of the vertices (x_i, y_i, z_i) and lists of the four cells [a_i, b_i, c_i, d_i] around each vertex i ($i = 1, 2, \dots, n_v$) where n_v is the total number of vertices of the cell aggregate. The lists of the four cells are described in Appendix A in detail.

2.2. Three-dimensional vertex dynamics cell model

The vertices obey the equation of motion:

$$\eta \, dr_i/dt = -\nabla_i U \quad (i = 1, \dots, n_v), \quad (1)$$

where r_i is a three-dimensional position vector of vertex i , and ∇_i the nabla differential operator. The left-hand side of Eq. (1) represents a viscous drag which is proportional to the vertex velocity dr_i/dt , with a positive constant η (an analogue of the coefficient of viscosity). Vertices do not have mass (inertia) so the cells are completely damped. The right-hand side of Eq. (1) represents a potential force (driving force), which is minus the gradient of the potential U . The potential U (or free energy) includes various terms related to cell surface area, cell volume, and potential energy due to external forces, expressed in terms of vertex coordinates. Hence, U is a function of the vertex positions. The equation of motion (Eq. (1)) was obtained by modifying the vertex model, which was originally derived in a more general form for 2D grain growth (Kawasaki et al., 1989) and extended to 3D (Nagai et al., 1990; Fuchizaki et al., 1995). The viscous drag comes from energy dissipation associated with interface motion. We assumed the coefficient η is constant because the circumference around vertex i does not extremely differ from each other (Nagai and Honda, 2001).

In this paper, the potential U usually contains two terms, U_s and U_v , and sometimes additional terms, U_z and U_{floor} . The potential U_s denotes the total surface energy of the cells:

$$U_s = \sigma \sum_f S_f + \sigma_o \sum_m S_m \quad (2)$$

($f = 1, 2, \dots, n_f$; $m = 1, 2, \dots, n_m$).

The first and second terms in Eq. (2) are the interface energy between neighboring cells and the surface energy between cells and the external culture medium, where n_f and n_m are the number of polygons facing an adjacent cell and facing the external culture medium, respectively. S_f is the surface area of a polygon f facing adjacent cells and σ its interface energy per unit area. S_m is the surface area of a polygon m facing the external culture medium and σ_o its surface energy per unit area. We can compute the areas of interfaces S_f and surfaces S_m , by triangulation of polygons. In cell aggregates without external culture medium (i.e. with periodic boundary conditions), the right-hand side of Eq. (2) lacks the second term.

The potential U_v denotes the total energy of cell compression and expansion:

$$U_v = \kappa \sum_{\alpha} (V_{\alpha} - V_{std})^2, \quad (\alpha = 1, 2, \dots, n), \quad (3)$$

where κ is a positive constant (an analogue of the elastic constant) and n the total number of cells. V_{α} is the volume of cell α and V_{std} is the volume of relaxed cells, defined as the average volume of all cells. Eq. (3) gives a

cell volume constraint. The role and form of such an area constraint have been discussed in a 2D soap froth (Weaire and Kermode, 1983, 1984; Wejchert et al., 1986), in magnetic froth (Weaire et al., 1991), and used to describe dynamical behaviors of biological cells in the extended Potts model (Graner and Glazier, 1992; Glazier and Graner, 1993).

To describe the experiment of flattening a cell aggregate under centrifugal force or gravity, we introduce two additional terms U_z and U_{floor} in the potential U :

$$U_z = \rho \sum_{\alpha} V_{\alpha} z_{\alpha}, \quad (4)$$

and,

$$U_{floor} = w_{floor} \sum_{\alpha} 1/[1 + \exp(az_{\alpha})], \quad (5)$$

where U_z is the potential energy induced by centrifugation. A body (mass m) in a centrifugation tube experiences a centrifugal force $m\omega^2(R - z)$, where ω is the angular velocity, R is the centrifugation radius at the bottom floor of the tube, and z is the distance of the body from the bottom floor. When R is much larger than z , the centrifugal force is approximately $m\omega^2 R$ ($= mg_C$ where g_C is the centrifugal acceleration, $\omega^2 R$). Then, centrifugation gives the body a potential energy, $mg_C z$. Therefore, the cell α with mass m_{α} has a potential energy $m_{\alpha} g_C z_{\alpha}$ where z_{α} is the z -coordinate of the center of mass of the cell. If the mass density of the cells under the centrifugal force is uniform, then the potential energy of cell α can be written as $\rho V_{\alpha} z_{\alpha}$, with $\rho = (\text{mass density}) \times g_C$, which leads to Eq. (4). U_{floor} expresses the hindrance of downward motion of cells along the z -axis by the floor below the cell aggregate. Cell α moves without restriction when it is above the floor ($z_{\alpha} > 0$), while it produces a large potential energy when it crosses below the floor ($z_{\alpha} < 0$). Instead of a step function, for example, $\{= 1, z_{\alpha} < 0; = 0, z_{\alpha} > 0\}$, we use an analytic function $1/[1 + \exp(az_{\alpha})]$. In Eq. (5), a is the slope of the approximated step function, and w_{floor} is the strength of the potential. Then Eq. (1) takes the form:

$$\eta \frac{dr_i}{dt} = -\nabla_i \left\{ \sigma \sum_f S_f + \sigma_0 \sum_m S_m + \kappa \sum_{\alpha} (V_{\alpha} - V_{std})^2 + \rho \sum_{\alpha} V_{\alpha} z_{\alpha} + w_{floor} \sum_{\alpha} 1/[1 + \exp(az_{\alpha})] \right\}. \quad (6)$$

We introduce a new length unit R_0 and rewrite Eq. (6) using new dimensionless quantities r'_i , $\nabla'_i (= \partial/\partial r'_i)$, S'_f , S'_m , V'_{α} , V'_{std} and z'_{α} as follows:

$$r_i = r'_i R_0, \quad \nabla_i = \nabla'_i / R_0, \quad S_f = S'_f R_0^2, \quad S_m = S'_m R_0^2, \\ V_{\alpha} = V'_{\alpha} R_0^3, \quad V_{std} = V'_{std} R_0^3, \quad z_{\alpha} = z'_{\alpha} R_0. \quad (7)$$

Using Eq. (7), Eq. (6) takes the form:

$$\frac{dr'_i}{dt'} = -\nabla'_i \left\{ \sum_f S'_f + \sigma'_o \sum_m S'_m + \kappa' \sum_{\alpha} (V'_{\alpha} - V'_{std})^2 + \rho' \sum_{\alpha} V'_{\alpha} z'_{\alpha} + w'_{floor} \sum_{\alpha} 1/[1 + \exp(d' z'_{\alpha})] \right\}, \quad (8)$$

where we define the new dimensionless quantities,

$$t' = t\sigma/\eta, \quad \sigma'_o = \sigma_o/\sigma, \quad \kappa' = R_0^4 \kappa/\sigma, \quad \rho' = R_0^2 \rho/\sigma, \\ w'_{floor} = R_0^{-2} w_{floor}/\sigma, \quad d' = a R_0. \quad (9)$$

We take $R_0 (= V_{std}^{1/3})$ so that $V'_{std} = 1$. Eq. (8) lacks explicit parameters corresponding to η and σ , since we want the vertex velocity, dr'_i/dt' and the interfacial tension to balance, $-\nabla'_i \sum_f S'_f$ without coefficients in the dimensionless form, because the interfacial tension is the main driving force. Without loss of generality, we can describe cell behaviors using the dimensionless parameters $\sigma'_o, \kappa', \rho', w'_{floor}$ and d' . Below, cell motions are measured in terms of the new length unit $R_0 = V_{std}^{1/3}$ and the new time unit η/σ , which are the characteristic length scale and time-scale of the cell aggregate, respectively. Hereafter, we omit primes ($'$) on the rescaled quantities in Eq. (8). For cell aggregates without centrifugation, we have

$$\frac{dr_i}{dt} = -\nabla_i \left\{ \sum_f S_f + \sigma_o \sum_m S_m + \kappa \sum_{\alpha} (V_{\alpha} - 1)^2 \right\}. \quad (10)$$

For cell aggregates under centrifugal force, we have

$$\frac{dr_i}{dt} = -\nabla_i \left\{ \sum_f S_f + \sigma_o \sum_m S_m + \kappa \sum_{\alpha} (V_{\alpha} - 1)^2 + \rho \sum_{\alpha} V_{\alpha} z_{\alpha} + w_{floor} \sum_{\alpha} 1/[1 + \exp(az_{\alpha})] \right\}. \quad (11)$$

In addition to the equations of motion, our model involves an elementary process of reconnection of neighboring vertices. When the length of an edge connecting two neighboring vertices is short (less than a critical length δ), the neighbors reconnect as shown in Fig. 2a, and the neighbor relationships of the vertices changes. The reconnection is an extension of the procedure of reconnection of neighboring vertices usually performed in 2D cellular patterns, e.g. Figs. 2 and 7 in Honda et al. (1982). Other reconnections are possible in general networks consisting of vertices with four edges (Wooten et al., 1985; Wooten, 2002), but our network is based, not on edges, but rather on faces composed of cell membrane.

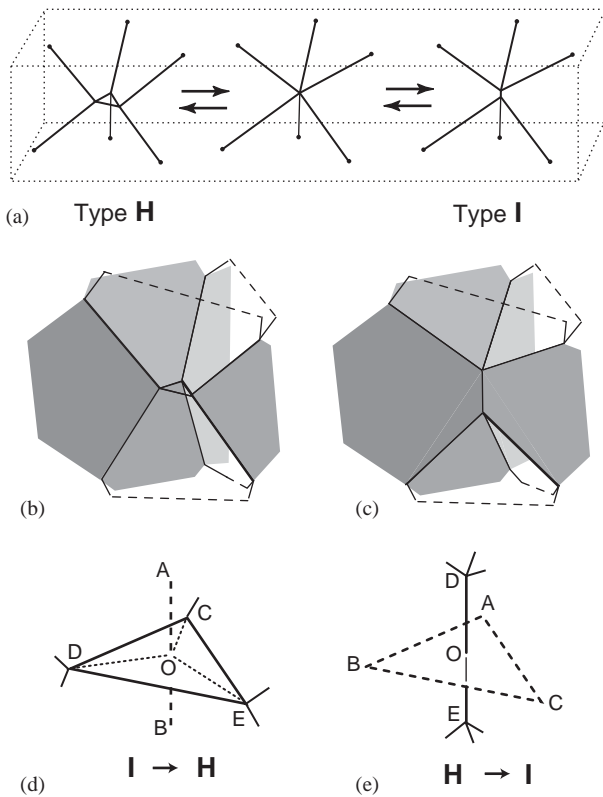


Fig. 2. Reconnection of neighboring vertices in a 3D tessellation consisting of faces. (a) Presentation by lines. When a triangle or an edge length is small, vertex topological connections of type H (left) and type I (right) are interchangeable. (b) Type H configuration presented by faces. Type H consists of 10 faces, three upper faces, three lower faces, three side faces and a face of small triangle. (c) Type I configuration presented by faces. Type I consists of 9 faces, three upper faces, three lower faces and three side faces. (d, e) Reconnection of vertices from type I to type H and from type H to type I, respectively. For details see Appendix B.

2.3. Computer simulations

2.3.1. Initial structure of computer simulations under periodic boundary conditions

To construct the initial structure, we use a 3D Voronoi tessellation (Tanemura et al., 1983; Tanemura, 1988, 1992). We consider two kinds of initial structures. In the first structure we distribute hard spheres of radius r (the number of spheres is n) in a random sequential packing within a box with periodic boundary conditions: we sequentially assign 3D coordinates to spheres using random numbers. If a new sphere overlaps with any existing sphere, we discard the coordinates and pick new ones. The process is repeated until the number of spheres reaches n . Of course, we assume the number of packed spheres is below the jamming limit. In the second structure, we put n hard spheres of radius r in a body-centered-cubic (b.c.c.) arrangement within a box with periodic boundary conditions. Based on the distributions of the centers of spheres thus obtained, we divide

the box into Voronoi domains, where two neighboring cells have a flat boundary face, which is perpendicular to a line segment connecting the cell centers, and located at the segment midpoint (Tanemura et al., 1983). Voronoi domains are all convex polyhedra. We choose the box size of the simulation so that the average cell volume is 1 as in Eqs. (10) and (11). We then calculate the coordinates of vertices x_i, y_i, z_i and determine the four-cell lists $[a_i, b_i, c_i, d_i]$ (See Appendix A) around each vertex i ($i = 1, 2, \dots, n_v$) according to the standard Voronoi tessellation (Tanemura et al., 1983). Thus, we can describe the initial structure by vertex coordinates and four-center lists around the vertices, instead of a distribution of the centers of the spheres. Starting with these initial structures, we perform the computer simulations by calculating vertex coordinates and four-cell lists around the vertices at each step. All boundary faces of Voronoi tessellations are flat. After the initial step, cellular structures generally deviate from Voronoi tessellations, but boundary faces did not deviate greatly from a flat plane because the boundary area of faces is minimized.

2.3.2. Vertex dynamics

We calculate each cell–cell boundary surface area (S_f) and each cell volume (V_α) from the vertex coordinates and the four-cell lists around the vertices, to obtain the potential (U) and its partial derivatives with respect to x_i, y_i , and z_i ($\nabla_i U$). We use the Runge–Kutta method with step size h (Ohno and Isoda, 1977) to calculate movements of all vertices by solving the equations of motion (Eqs. (10) or (11)) simultaneously. After each Runge–Kutta time step, we perform the elementary process of reconnection as follows.

2.3.3. Reconnection of neighboring vertices

[Step a]. We calculate all edge lengths, and list edges with lengths shorter than the critical length δ in order of ascending length.

[Step b]. We pick edges ij sequentially from the list of short edges. If the vertex i or j connects to edges that have already reconnected, we skip it, and repeat Step b for the next edge in the list. Otherwise, we count how many triangles the edge belongs to. In general, each edge belongs to three polygons (see Fig. 1b). If none of the three polygons is a triangle, the edge is type I (Fig. 2c). We reconnect from type I to type H as shown in Fig. 2d, then repeat Step b. If one of the three polygons is a triangle, the edge is type H (Fig. 2b). We reconnect from type H to type I as shown in Fig. 2e, then repeat Step b. If two or more of the three are triangles, we skip the edge and repeat Step b. When we have reconnected all edges in the list, the step ends. The next step begins with the Runge–Kutta calculation of the coordinates of the vertices using the equations of motion (Eqs. (10) or (11)). Simulation time t equals $h \times (\text{step number})$. We

repeat this procedure until $t = 10\text{--}200$ (see each simulation) at which point the polygonal patterns almost do not change.

2.3.4. Initial structures for computer simulations of cell aggregates

To construct the initial structure to simulate a cell aggregate, we distribute 430 hard spheres (radius $r = 0.45$) at random in a cube of edge length 7.548 (its volume is 430) using periodic boundary conditions. We described our method for the distribution of hard spheres at random in Section 2.3.1. From the distributed spheres we construct the Voronoi tessellation and evolve it using the vertex dynamics (Eq. (10)) for a short time until $t = 1$ (2000 steps) under periodic boundary conditions, to obtain a partially relaxed structure derived from the Voronoi pattern through reconnection of neighboring vertices under minimization of boundary face areas. The number of vertices in the system, $n_v = 491$. From the system of 430 cells in a cube, we constructed a cell aggregate of a radius of approximately 2.9, as described in Appendix C.

2.3.5. Flatness of a polyhedron

We define the degree of flatness of a polyhedron in the z -direction as follows:

$$\text{Flatness} = \sum_i \{(x_i - x_G)^2 + (y_i - y_G)^2\} / \sum_i (z_i - z_G)^2, \quad (12)$$

where (x_G, y_G, z_G) is the center of mass of the polyhedron, and summations are over all polyhedron vertices. Flatness is sensitive to the shape of the polyhedron, because for flatter polyhedra, the denominator of Eq. (12) becomes small. Flatness does not diverge since polyhedral cells always have finite volumes in the simulations. Note that a cube, a typical roundish (or isodiametric) polyhedron, has $\text{flatness} = 2$.

2.3.6. Parameter values used in the simulations

We do not have accurate values for the parameters related to cell properties at present. Thus, the present paper investigates general behaviors of polyhedral cells in typical cell aggregates using Eqs. (10) or (11) with dimensionless parameter values. σ_o is now the ratio of the cell-medium boundary energy density to the cell-cell boundary energy density (Eq. (9)). σ_o determines the shape of cell aggregates under centrifugal force. Our preliminary simulations showed that when σ_o varied from large to small value, the aggregate changed from a sphere to an ellipsoid and then to a cap-shaped body on the floor under a centrifugal force of constant strength ρ . We chose σ_o so that the aggregate became ellipsoidal ($\sigma_o = 5$). For $\sigma_o = 2.5$ the cell aggregate became cap-shaped and collapsed. When κ , the coefficient of cell compression or expansion energy, was large, the cells in

the aggregate did not change their shape. However, when κ decreased, some cells collapsed and became concave polyhedra. We then chose κ so that the aggregate became flat under centrifugal force ($\kappa = 5$). The value of ρ is proportional to the magnitude of centrifugation. Since a typical centrifugal acceleration is $g_C = 1000\text{--}12\,000\,g$ (where g is the gravitational acceleration) according to Phillips and Steinberg (1978), we can neglect the effect of gravitational force on cell behavior. We also used $\rho = 1$ for simulations including centrifugal force, which means that the centrifugal force and the interfacial tension have the same order of magnitude. The last term on the right-hand side of Eq. (11) simulates the rigid substrate. Its parameters w_{floor} and a have a wide allowed range. We used $w_{\text{floor}} = 0.5$ and $a = 100$. The critical length for reconnection δ is the lower cutoff length in the model, and should be small for detailed description. However, if it is too small in complicated tessellation patterns, the process is frozen. We used $\delta = 0.025$ or 0.05 , where cell volume (V_{std}) is 1. The step size h for the Runge-Kutta method was $0.002\text{--}0.02$. We will describe the values of δ and h to each simulation.

2.3.7. Computation

We made computer programs in FORTRAN 77 and used them on workstations (AS7000 U1E/170, Toshiba Co., Japan; Octane-R12000, Silicon Graphics Inc., USA) at Hyogo University and a digital super computer (Hitachi SR8000, Hitachi Co., Japan) at the Institute of Statistical Mathematics. For display and analysis, we used personal computers (Power Macintosh 7500/100 or Power Mac G4, Apple Co., USA) with mathematics and graphics software (Mathematica ver. 2.2, Wolfram Research Inc., USA and Adobe Illustrator 5.5J, Adobe Systems Inc., USA).

3. Results

We first examined the minimal surface problem using the vertex dynamics of Eq. (10). We required that all edges were straight (not curved. See Appendix D). Among straight edged polyhedra identical in shape and size and fill 3D space without gaps or overlaps, the orthic tetrakaidecahedron has the least surface area (Weaire and Phelan, 1996). This polyhedron is the Voronoi cell of the b.c.c. structure and has six square faces and eight hexagonal faces. A Voronoi tessellation with centers arranged in a b.c.c. structure generates an orthic tetrakaidecahedral tessellation, which did not change under the vertex dynamics (Fig. 3a). The boundary area of this tessellation did not decrease, so it was at least a local minimum energy configuration. Fig. 3b shows the deformed pattern when we displaced one of the Voronoi centers by 0.8, where the nearest

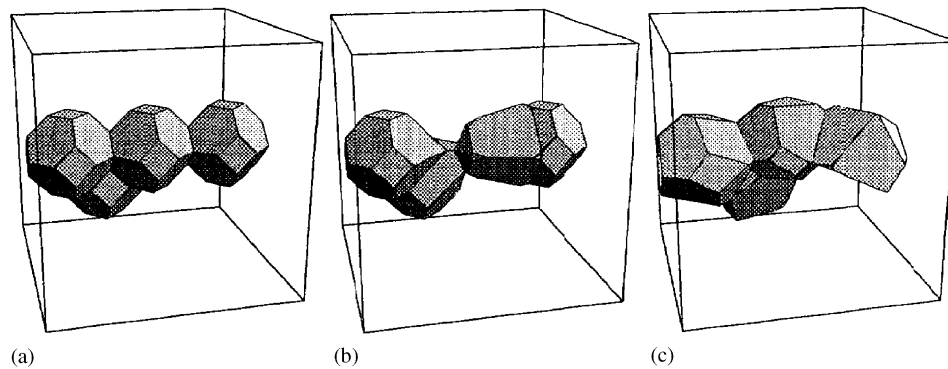


Fig. 3. Polyhedral patterns produced by computer simulations under vertex dynamics (Eq. (10)) with periodic boundary condition on a cube. Step size in the Runge–Kutta calculation $h = 0.02$. Critical edge length, $\delta = 0.05$. $\kappa = 5$. For simplicity, we show only four cells. (a) Orthic tetrakaidecahedra. Voronoi tessellation of a b.c.c. arrangement of centers ($n = 54$) in the cube (length of box edge = 3.78). (b) Initial condition: b.c.c. with nearest neighbor distance 1.09 with one center displaced towards the x -axis (abscissa) by 0.8. (c) Initial condition: b.c.c. with nearest neighbor distance 1.09 with all centers displaced randomly along each axis in the range -0.3 to $+0.3$.

neighbor distance in the b.c.c. was 1.09. Under the vertex dynamics ($t = 30$), the deformed polyhedra recovered the tetrakaidecahedral structure of Fig. 3a through vertex reconnection around the displaced Voronoi center. If we disturbed the positions of all Voronoi centers at random (displacing along each axis by -0.3 to $+0.3$), the resulting Voronoi tessellation was irregular as in Fig. 3c, with no tetrakaidecahedra. Under the vertex dynamics ($t = 80$), the deformed polyhedra recovered the tetrakaidecahedra of Fig. 3a through vertex reconnection. Thus the vertex dynamics including vertex reconnection can reduce the interface energy of cells.

Next, we examined a cell aggregate. We constructed an initial cell aggregate of 105 polyhedra as described in Section 2.3.4. The vertex dynamics produced a spherical cell aggregate using Eq. (10) ($t = 10$; Figs. 4a and b). Then, exposing the cell aggregate to centrifugal force using Eq. (11) flattened the cell aggregate as shown in Figs. 4c and d. The cells first did not rearrange. The relative positions of the cells in the aggregate at early stages were similar to those of the initial cell aggregate (compare the cells in Fig. 5b with those in Fig. 5a). Subsequent application of centrifugal force rearranged the cells as shown in Fig. 5c, although the shape of the whole cell aggregate did not change. After we removed the centrifugal force, the cell aggregate began to recover its original shape (Fig. 5d), and finally became completely spherical (Fig. 5e). The individual cells elongated vertically without rearrangement (Fig. 5d), then rearranged (Figs. 5d–e). We traced three neighboring cells in the simulation shown in Fig. 5 and obtained their snap shots in Fig. 6. The top and bottom cells, which were initially separate (Figs. 6a and b) came into contact (Fig. 6c), and again the top and bottom cells separated as in Fig. 6e.

Fig. 7 shows quantitatively the change in cell and aggregate shapes characterized by the flatness as defined by Eq. (12). Fig. 7a shows a schedule of application of

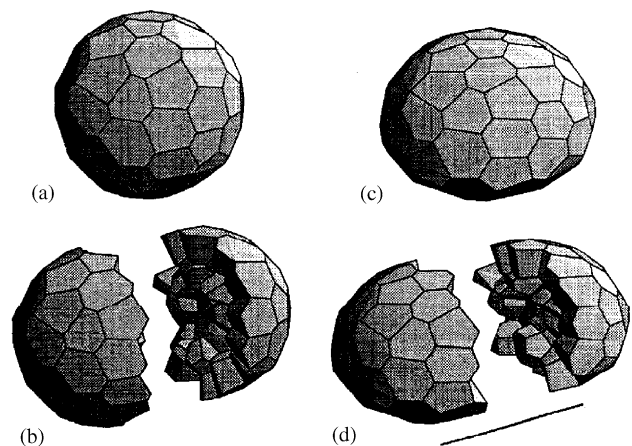


Fig. 4. A computer simulation of centrifugal flattening of an aggregate using Eq. (11). An initial cell aggregate (radius $r = 2.9$) was produced as described in Section 2.3. Number of cells, $n = 105$. Critical edge length for reconnection, $\delta = 0.05$. Step size in the Runge–Kutta calculation, $h = 0.002$. Parameters, $\sigma_o = 5$ and $\kappa = 5$. Bar length 5.0. (a) A cell aggregate at $t = 10$ without centrifugation ($\rho = 0$, and $w_{\text{floor}} = 0$). (c) A cell aggregate at $t = 12$ with centrifugation. The cell aggregate of figure (a) was simulated for $t = 0$ –12 under centrifugal force ($\rho = 1$, and $w_{\text{floor}} = 0.5$). (b) and (d) show the interiors of cell aggregates (a) and (c), respectively.

centrifugation force. The centrifugation stopped at $t = 24$ (arrow in Fig. 7a). The flatness of the cell aggregate increased and returned to the initial value (open squares in Fig. 7b). However, while the individual cells (solid circles in Fig. 7b) also flattened like the whole aggregate under centrifugation, they returned to spherical (isodiametric) shapes around $t = 12$. This recovery was observed experimentally by Forgacs et al. (1998). When centrifugation was removed at $t = 24$ (arrow in Fig. 7a), the cells (solid circles in Fig. 7b) suddenly decreased their flatness, became spherical and then elongated (flatness less than 2), and gradually recovered their original round shape. The behavior of the individual

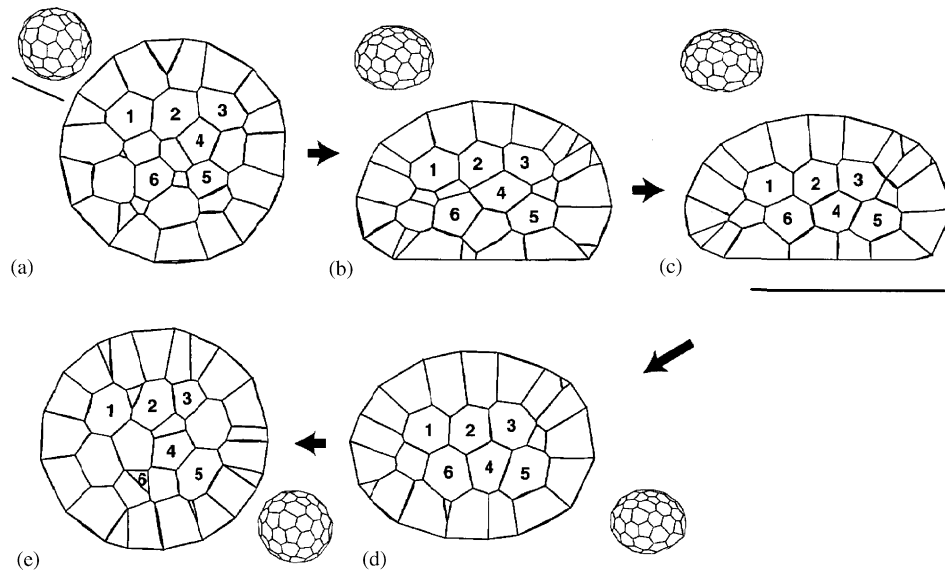


Fig. 5. Sections through a cell aggregate during application and removal of centrifugal force. The initial cell aggregate was produced as described in the legend of Fig. 4a. Number of cells, $n = 105$. Critical edge length for reconnection, $\delta = 0.05$. Step size in the Runge–Kutta calculation, $h = 0.002$. Parameters, $\sigma_o = 5$ and $\kappa = 5$. Bar length 5.0. Inset, views of entire aggregates at corresponding times (the small bar has a length of 5.0). (a) Initial structure ($t = 0$) to which the centrifugal force is applied ($\rho = 1$ and $w_{floor} = 0.5$). The same conditions as in Fig. 4a. (b) $t = 12$. (c) $t = 24$ at which time the centrifugal force is removed ($\rho = 0$ and $w_{floor} = 0$). (d) $t = 26$ ($t = 2$ after the removal of the centrifugal force). (e) $t = 54$ ($t = 30$ after the removal of the centrifugal force).

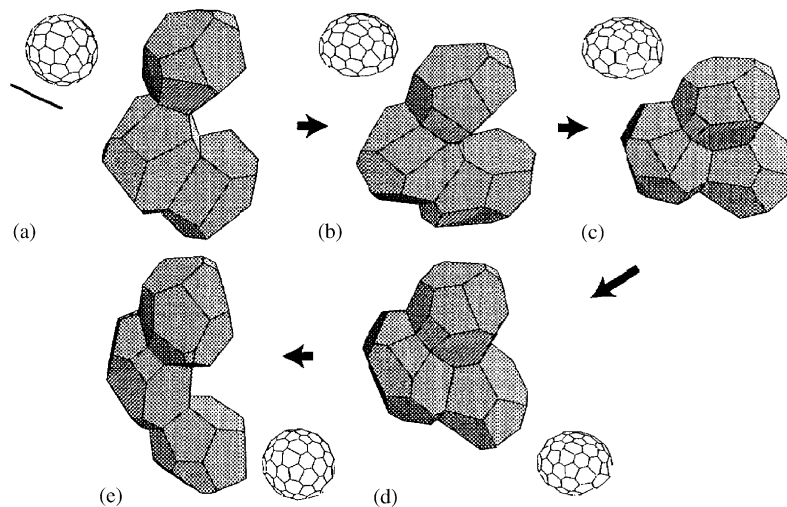


Fig. 6. Behaviors of three cells in a cell aggregate during changes in centrifugation. (a, b, c, d, e) and Inset show the same conditions as in Fig. 5.

cells depended not only on the cell aggregate shape, but also on their relaxation time. This result demonstrates viscoelastic properties of the cell aggregate based on the deformation and rearrangement of component cells, which have been investigated in several works (Phillips et al., 1977; Phillips and Steinberg, 1978; Phillips and Davis, 1978; Forgacs et al., 1998; Beysens et al., 2000).

Fig. 7b (solid line) shows the average shape change of individual cells. In comparison with the experimental result (Figs. 3 and 4 in pp. 129–130 in Phillips et al.,

1977), the actual morphological change of individual cells was more remarkable than the simulation result. In the simulation, the surface of the aggregate facing the culture medium influenced the shape of the cells within the aggregate. Fig. 5a shows that polyhedral cells that contacted the culture medium (surface cells) had irregular shapes (elongated towards the surface of the aggregate), while cells contacting only other cells (inner cells) were isodiametric. Our simulated aggregate contained only 105 cells, so the ratio of surface cells to inner cells was about 5:2. In contrast, the number of

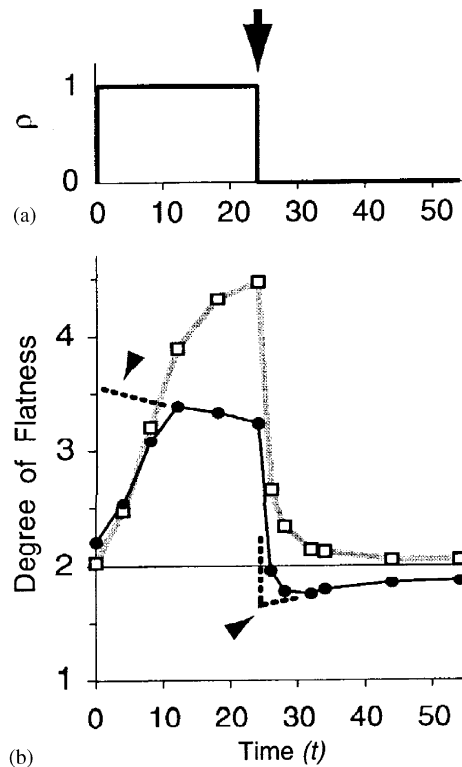


Fig. 7. Shape changes of the cell aggregate and individual cells in the simulation of Fig. 5. Abscissa, simulation time (t). (a) Application of stress by centrifugation. Ordinate, ρ , which is proportional to the centrifugal force acting on a unit volume of a cell (see text). Centrifugation was applied at $t = 0$ and removed at $t = 24$ (arrow). (b) Open squares, flatness of the cell aggregate obtained by Eq. (12). Solid circles, average flatness of the cells. First, flatness of each cell within the aggregate was obtained by Eq. (12), then the flatnesses of all cells were averaged. Dotted lines with arrowheads indicate difference from the analytic results as shown by gray line in Fig. 9c.

cells in an actual cell aggregate is much larger and most cells are far from the aggregate surface. We simulated this situation using a periodic boundary condition (simulating an infinite system of cells) as shown in Fig. 8a. We then compressed the box height by $2/3$, keeping the box volume constant (Fig. 8c). The vertex dynamics shaped the aggregate as shown in Fig. 8e at $t = 200$. Figs. 8b, d and f show cross sectional views of Figs. 8a–c, respectively. Roundish cells initially (Fig. 8b) flattened remarkably after the compression (Fig. 8d), then recovered nearly to their original shapes (Fig. 8f).

4. Discussion

4.1. Polyhedral cells and cell aggregate

A biological cell is multi-potent. It contains a complete set of genes, reproduces itself, obtains energy and materials for itself through metabolic pathways, changes its shape, senses and responds to external

stimuli, migrates, and even dies if necessary. However, body formation consists of many morphogenetic steps by individual cells, and cells at each step use only a few of their abilities. Which abilities are necessary for which steps of morphogenesis? A dynamic cell model should give an insight into the question.

A cell aggregate reflects the properties of its component cells and in turn influences their properties. Cells can maintain a constant volume (Okada, 1997; Lang et al., 1998), and minimize surface area. Taking into consideration these properties of cells into our model, our simulations show: (1) A cell aggregate in free space rounds up as shown in Figs. 4a and 5e. (2) The interfaces between cells in an aggregate remain flat. Although vertices in 3D connected with straight edges do not necessarily form planar polygons (e.g. boat or chair conformation of cyclohexane C_6H_{12}), surface minimization maintains planar faces (Fig. 6). (3) Polyhedral cells can move in a dense cell aggregate, even in the absence of spaces between cells. When cells are arranged in a 2D plane, they easily migrate because they have a free space above their apical surface and can elongate vertically if necessary for their movement. In contrast, cells in a 3D aggregate do not have such free space. The 3D vertex dynamics model explicitly showed that cell movement in a 3D aggregate is possible. The cell movement belongs to slippage as mentioned in Phillips et al. (1977) resulting in rearrangement of neighboring cells. [Cell migration over distances of many cell diameters in a 3D cell aggregate has been shown by the 3D extended Potts model (Mombach et al., 1995). The cell migration was caused by repetition of cell rearrangements. The rearrangements in the 3D extended Potts model are described by changes of spin values at respective lattice sites]. Finally, (4) surface minimization by cells helps to drive cell movement and influences the properties of the aggregate (see Section 4.4).

4.2. The polyhedral cell models in a 3D aggregate

We summarize here polyhedral cell models for investigation of cell shapes, deformation and rearrangement in a 3D cell aggregate. The topological dynamics cell model (Dubertret and Rivier, 1997, 2000) is two-dimensional. Even if it is extended to three-dimensions, it cannot provide vertex coordinates for the polyhedra. The center dynamics model is based on the positions of cell centers. Description of cell positions by centers is simple and easy to understand. Especially for complex systems containing many cells, the center dynamics model is useful and frequently used as mentioned in Section 1. (Honda et al., 1996; Clem et al., 1997; Bretschneider et al., 1999; Palsson and Othmer, 2000; Palsson, 2001). To examine the shapes of individual cells in a tissue, however, we have a problem. The cell center does not necessarily correspond to actual material and,

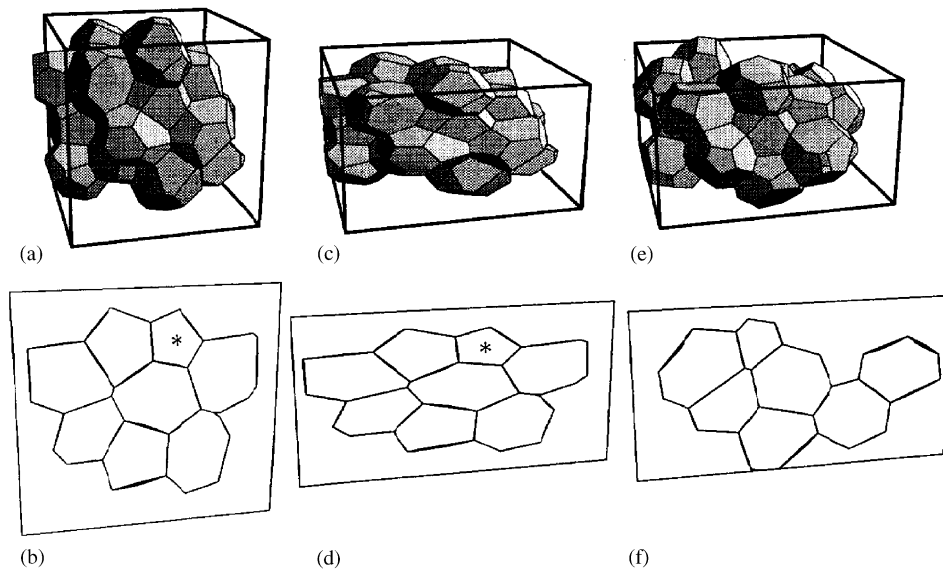


Fig. 8. Simulation of cell flattening and recovery for periodic boundary conditions. Critical edge length for reconnection, $\delta = 0.025$. Step size in the Runge–Kutta calculation, $h = 0.005$. For simplicity, we draw only selected central cells. Parameter values in Eq. (10) $\sigma_o = 1$, $\kappa = 5$. (a) $t = 50$. The initial condition was a Voronoi tessellation: Spheres (radius $r = 0.45$, number $n = 54$) were distributed at random in a cube of edge length 3.78 with periodic boundary conditions (see Section 2.3). Under the vertex dynamics, the cells relax towards roundish and isodiametric irregular polyhedra (not tetrakaidecahedral). (c) The z -coordinates in figure (a) were reduced by 2/3, and the x - and y -coordinates increased so that the boundary volume remained constant (the box size is $4.63 \times 4.63 \times 2.52$). (e) $t = 200$ after figure c under the same conditions as figure (a). (b, d and f) Sections of figures (a), (b) and (c), respectively. The cell marked by an asterisk in figures (b) and (d) disappeared by moving vertically out of the sectional plane in figure (f).

especially in a cell aggregate, we can only determine the positions of cell centers for polygonal or polyhedral cells with difficulty. The Voronoi construction gives the positions of vertices only approximately (e.g. Honda, 1978; Graner and Sawada, 1993). Cell boundaries in real aggregates, however, are material made of cell membranes, and the positions of vertices are determined by the contact between cell boundaries. The cell boundaries are tensile (Owaribe et al., 1981; Owaribe and Masuda, 1982). Two neighboring edges meet at a vertex at an angle as close to 120° as possible in 2D (Honda and Eguchi, 1980; Honda et al., 1982, 1983). In 3D, the angle around a vertex is expected to be $109^\circ 28'$, the tetrahedral angle under boundary minimization (Weaire and Phelan, 1996). Center dynamics cannot explicitly describe these geometrical properties of boundaries and vertices. Indeed, Honda et al. (1983) showed deviation from Voronoi domains in the blastula wall of the starfish by investigating the relation between Voronoi domains in the center dynamics model and contracted boundary polygons in the vertex dynamics model.

The extended Potts model is a boundary dynamics model that describes cell patterns by the shape of their boundaries (many lattice points along boundaries). The model that had been used for physical systems was developed by Graner and Glazier to describe biological systems in two dimensions (Graner and Glazier, 1992; Glazier and Graner, 1993), and later extended to three dimensions (Mombach et al., 1995). The model does not

make an assumption about edge and face shapes. Curved faces and edges could be included if the computer's memory capacity is sufficient (see Appendix D). Since the algorithm in the model is rather simple, the model is extensively used for biological organisms (Savill and Hogeweg, 1997; Mombach et al., 2001; Marée and Hogeweg, 2001, 2002). The extended Potts model, however, employs a discrete lattice to represent continuous space. The model is not convenient to present cells visually, since the computer capacity limits the number of lattice sites and reduces accuracy. With regard to cell dynamics, cell movement in cell aggregates has been quantitatively observed and analyzed (Upadhyaya et al., 2001). The Potts model itself does not directly treat cell dynamics, but is usually used with Monte Carlo dynamics. The unit of time, a Monte Carlo step (MCS) is taken as a certain number of attempts to change each lattice site, so the time-scale must be adjusted to agree with real processes (Mombach et al., 2001).

The 3D vertex dynamics in the present paper easily provides vertex positions and boundary faces, and is convenient to visually present polyhedral cell shapes. The model has a characteristic time-scale η/σ given by Eq. (9), which combines two material constants. The coefficient of viscous drag η and the interfacial tension σ can be determined independently by dynamic and static measurements, respectively. When experiments provide these material constants, the vertex dynamics specify a time-scale by which it can be tested.

4.3. Minimization of the potential U and the role of the elementary process of reconnection

We note that the equation of motion in Eq. (1) expresses completely dissipative vertex motion under the potential U . Differentiation of the potential U with respect to time t gives the following inequality (using Eq. (1)):

$$dU/dt = \sum_i dr_i/dt \nabla_i U = -\eta \sum_i (dr_i/dt)^2 \leq 0. \quad (13)$$

The inequality indicates that vertices move to decrease U (or not to increase U). For example, if U is the total surface area of cell boundaries, the vertices move to reduce the total surface area. Note that Eq. (13) is deterministic. The vertices follow the gradient of the position-dependent energy, so the cells passively change their shape to satisfy Eq. (13). Without the reconnection of neighboring vertices, the evolving pattern according to Eq. (1) preserves its initial topology, which is not the case of interest. In contrast, the vertex dynamics model reconnects neighboring vertices (topological change) when an edge length is less than δ . The length δ is the minimum length, or the lower cutoff length in our coarse-grained model. The inequality Eq. (13) holds during each interval between two successive topological changes (Fig. 2a), while each change gives rise to a small jump in U . The jump in U is $\sigma\Delta S$ where ΔS is the change of surface area in the jump and is of the order of $\delta \times (\text{average length of edge})$. Then the jump in U is of the order of $\sigma\delta \times (\text{average length of edge})$ and can be neglected. We can regard the potential U as an approximately decreasing function of time. The elementary processes allow vertices to escape from metastable local minimum traps. We do not consider any fluctuations in cell movement coming from thermal noise or from active cell motility through the consumption of metabolic energy. We will include thermal noise and active cell movements in the future.

4.4. Viscoelastic cell aggregates

When cell aggregates undergo mechanical deformation, they relax like elastic materials on short time-scales and like viscous liquids on long time-scales (Phillips et al., 1977; Phillips and Steinberg, 1978; Phillips and Davis, 1978; Forgacs et al., 1998; Beysens et al., 2000). The viscoelastic properties of the cell aggregate have been extensively studied and discussed (Foty et al., 1995, 1996; Beysens et al., 2000; Palsson, 2001). Our simulations, which assumed minimization of cell surface area, exhibited cell behaviors in an aggregate (Figs. 5 and 6), and quantitatively showed shape changes of cells and the aggregate (Fig. 7). We will discuss the viscoelastic properties of an aggregate with regard to cell rearrangement caused by a motive force provided by cell interface

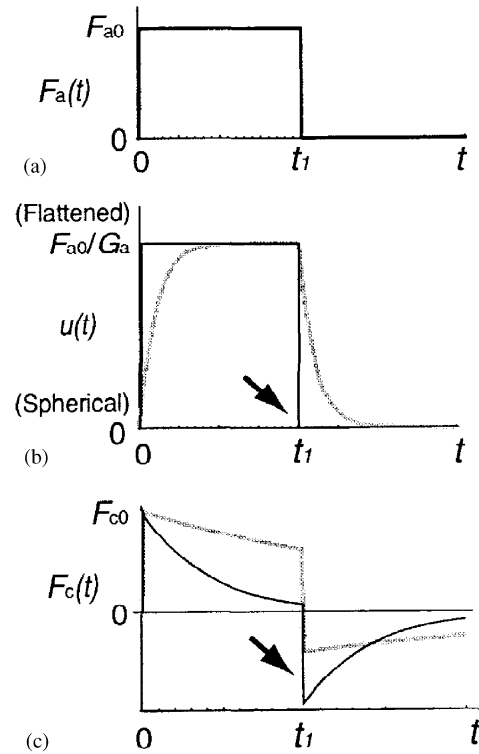


Fig. 9. Stress and deformation of a cell aggregate and individual cells by analytic calculations using the theory of viscoelasticity. (a) Stress on a cell aggregate. Stress (F_{a0}) is applied at $t = 0$, maintained constant and removed at $t = t_1$. (b) Deformation of the aggregate. We obtain the deformation (called *creep*) $u(t)$ from the Voigt model (e.g. Fung, 1981): $u(t) = F_{a0}/G_a[1 - \exp(-t/\tau_a)]$ for $t \leq t_1$, where the relaxation time of the aggregate deformation $\tau_a = \mu_a/G_a$, G_a is an elastic spring constant, and μ_a is the coefficient of viscosity for the dashpot. When the stress is suddenly released at $t = t_1$, the deformation of the aggregate obeys $u(t) = u(t_1) \exp[-(t - t_1)/\tau_a]$ for $t > t_1$, where $u(t_1)$ is obtained for $u(t)$ for $t \leq t_1$. Thin solid line: the perfect elastic case ($\tau_a = 0$). Gray line, viscoelasticity with relaxation time $\tau_a = 1$. (c) Stress on individual cells. When the aggregate is suddenly deformed as shown according to the thin solid line in figure (b) ($\tau_a = 0$), the stress $F_c(t)$ follows a Maxwell model (e.g. Fung, 1981): $F_c(t) = F_{c0} \exp(-t/\tau_c)$ for $t \leq t_1$, where the relaxation time of stress for cells $\tau_c = \mu_c/G_c$, G_c is an elastic spring constant, and μ_c is the coefficient of viscosity for the dashpot. When the aggregate suddenly recovers its original shape at $t = t_1$ (arrow in figure (b)), the stress is obtained as shown according to the thin solid line in figure (b) for $t > t_1$, where $F_c(t_1)$ is obtained from $F_c(t)$ for $t \leq t_1$. Thin solid line, stress for viscoelasticity with relaxation time ($\tau_c = 0.4$) for deformation of the aggregate ($\tau_a = 0$, solid thin line in figure (b)). Gray line, stress for viscoelasticity with a long relaxation time ($\tau_c = 2$) for the same deformation of the aggregate ($\tau_a = 0$, the solid thin line in figure (b)). Deformation of the individual cells is similar to figure (c), with F_c replaced by F_c/G_c .

minimization. Based on the theory of viscoelasticity, we performed the analytic calculation of a viscoelastic cell aggregate as described in the legend of Fig. 9, and our results are shown in Fig. 9. Figs. 9a–c show stress F_a on the aggregate (a), the deformation $u(= F_a/G_a)$ of the aggregate (b) and the stress F_c on the individual cells (c), respectively. We do not show the deformation of individual cells, since the change of deformation was similar to (c).

The change in the shape (flatness) of the aggregate in the simulation (gray line in Fig. 7b) is supported experimentally. It is close to the change in the roundness of the experimental aggregate of embryonic liver cells (Fig. 10 in p. 10 in Phillips and Steinberg, 1978). The flatness of our definition and the roundness of definition of the experiment (Phillips and Steinberg, 1978) both show the *creep* behavior of viscoelastic bodies (Fung, 1981), although these definitions differ because we define flatness by using the distribution of vertices while Phillips and Steinberg (1978) define roundness as the ratio of the height above the equator to the width at the equator of an aggregate.

The change in flatness of the aggregate in the simulation (gray line in Fig. 7b) corresponds to the analytical calculation (gray line in Fig. 9b). When stress (e.g. by centrifugation) was applied to the aggregate for a certain duration ($t = 0 - t_1$ in Fig. 9a), the aggregate, as shown in Fig. 9b, deformed from spherical to flattened shapes just after the stress started ($t = 0$), and recovered from flattened to spherical ones just after the stress ended ($t = t_1$). The thin solid line in Fig. 9b represents the case of a perfect elastic solid (relaxation time of deformation $\tau_a = 0$). The gray line in Fig. 9b represents deformation with a relaxation time ($\tau_a = 1$), which is similar to the simulation result of the gray line in Fig. 7b.

On the other hand, our simulation showed curious changes in the flattening and elongation of individual cells (solid line in Fig. 7b). We will discuss the curious changes with the aid of analytic calculation (Fig. 9c), since shape changes of individual cells are difficult to monitor experimentally. We consider two relaxations with a short relaxation time (τ_a) due to the elastic deformation of a cell aggregate and a long relaxation time (τ_c) due to the rearrangement of individual cells in the aggregate according to Forgacs et al. (1998). The aggregate was flattened as the thin solid or gray lines in Fig. 9b by an external force. Flattening the aggregate also compresses individual cells that experience stress F_{c0} (at $t = 0$ in Fig. 9c). However, the cells rearrange themselves to recover their original isodiametric shapes. During recovery, the stress on each cell decreases with relaxation time τ_c ($t = 0 - t_1$ in Fig. 9c). Based on the deformation of the aggregate with $\tau_a = 0$ (thin solid line in Fig. 9b) and assuming relaxation time due to cell rearrangement $\tau_c = 0.4$, we calculated the decrease of the stress and the result is shown by the thin solid line in Fig. 9c. The stress decreased until the cells within the flattened aggregate became isodiametric. Although the whole aggregate remained flat ($t \leq t_1$ in Fig. 9b), the cells within the aggregate became almost isodiametric. Removing the stress ($t \geq t_1$ in Fig. 9a), the flattened aggregate recovers its original spherical shape (arrow in Fig. 9b). Simultaneously, the isodiametric cells within the aggregate experience a tensile stress (i.e. extension)

and elongate (arrow in Fig. 9c). The elongated cells again rearrange to recover their original isodiametric shapes, decreasing the extension stress ($t > t_1$ in Fig. 9c).

Corresponding to the simulation result (solid line in Fig. 7b), we calculated the stress of individual cells assuming slower relaxation time due to cell rearrangement ($\tau_c = 2$). The analytic result is shown by gray line in Fig. 9c, which is similar to the simulation result. Differences of the simulation result from the analytic result are indicated by the dotted lines (arrowheads at $t = 0 - 10$ and $t = 24 - 30$ in Fig. 7b), which are due to the assumption that the aggregate is perfectly elastic (i.e. $\tau_a = 0$).

Quantitative comparison of the simulation results (Fig. 7) with the analytic results (Fig. 9) is difficult because the flatness in Fig. 7b is not proportional to the mechanical deformation in Fig. 9b. In addition, the solid line in Fig. 7b shows the average over all cells in the aggregate, which contains more surface cells than bulk cells as mentioned in Section 3 (the ratio is about 5:2), so the culture medium affects the shapes of the cells. Nevertheless, the analytic results in Fig. 9 help us to understand the flattening and elongation of individual cells (solid line in Fig. 7b).

The result of our computer simulation suggests that elastic deformation and minimization of cell surface area cause a bimodal relaxation, short term solid-like and long term liquid-like behaviors, as indicated by Forgacs et al. (1998). Tension of the cell boundary surface causes movement of cells in tissues. In our simulation using dynamic model of cells, we can recognize visually the shape changes and rearrangements of component cells that produce the properties of cell aggregate.

Acknowledgements

We thank anonymous reviewers for revising the paper. The results described in the present paper were obtained in part when H.H. was a Visiting Professor at the Institute of Statistical Mathematics, Tokyo, Japan (1997–1999). Supported by Japan JSPS.KAKENHI 09878173 and 13878156.

Appendix A. A method of describing polyhedra by vertex coordinates and their four-cell lists

Interfaces between neighboring cells and volumes of polygonal cells in the 3D cell model have to be expressed by vertex coordinates in the equation of motion (Eq. (1)). For this purpose, the neighboring relationship of vertices (i.e. an edge) is necessary, which is described by cells as follows: Three neighboring cells (α , β and γ determine an

edge (Fig. 1b). Two neighboring cells (α and β) determine a boundary surface between them (Fig. 1c).

The tessellation pattern of a cell aggregate is a structure consisting of straight lines, and is completely defined by the coordinates of the vertices (x_i, y_i, z_i) and lists of the four cells [a_i, b_i, c_i, d_i] around each vertex i ($i = 1, 2, \dots, n_v$) where n_v is the total number of vertices of the cell aggregate. Lists of the four cells (a four-cell list) around vertices define vertex relationships. For example, we compare two lists, [a_i, b_i, c_i, d_i] and [a_j, b_j, c_j, d_j] for vertices i and j . If the two lists for i and j show three common cells (e.g. cells α, β and γ), an edge defined by the three cells α, β and γ (Fig. 1b) directly connects vertices i and j . If two cells (e.g. cells α and β) are common, the two vertices i and j belong to a boundary surface between the two cells α and β (Fig. 1c). If one cell (e.g. cell α) is common, the two vertices i and j belong to a polyhedron of cell α (Fig. 1d). If the lists show no common cells, the two vertices are isolated from each other as shown in Fig. 1a. The cell identifications (e.g. cells $\alpha, \beta, \gamma, \dots$) define vertex relationships, but not the x -, y -, and z -coordinates of vertices.

Appendix B. Configuration of the reconnected neighboring vertices

The tessellation pattern of polyhedra in the 3D cell model is based not on edges but rather on faces composed of cell membranes. The reconnection of neighboring vertices is an interchange between Figs. 2b and c. The assumption of the quantitative configuration used in the simulation is as follows. Fig. 2d is reconnection of vertices from type I to type H. The broken line, AB, and solid lines, CD, DE, and EC, indicate initial and final patterns, respectively. Edge length AB is d . Radius of the circumscribed circle of a triangle CDE is $2d$, and its center O is the midpoint of edge AB. Directions of OC, OD and OE are determined by two tetrapods around A and B. Reconnection of vertices from type H to type I is Fig. 2e. Broken lines, AB, BC, and CA, and solid line, DE, indicate initial and final patterns, respectively. The minimum length among three edges AB, BC and CA is d . Edge DE is $2d$ in length and perpendicular to triangle ABC. The midpoint O of edge DE is the center of mass of the triangle ABC.

Appendix C. Vertex coordinates and their four-center lists of the cell aggregate

In Section 2.3.4, we constructed a system of 430 cells (491 vertices) in a cube. From this system, we made a cell aggregate expressed by vertex coordinates and their four-center lists as follows. We calculated all coordinates of the centers of mass of the polyhedra in the cube

and discard the centers (outside-centers) outside a large sphere (radius = 2.9). Then, 105 centers remain (inside-centers). Next, we define vertices in the cell aggregate. A vertex has its own four-center lists [a_i, b_i, c_i, d_i]. We discard vertices with lists containing two or more outside-centers. The remaining vertices have lists containing three or four inside-centers. We replace the outside-centers in the lists by a 106th center, which corresponds to a big polyhedron consisting of the union of 105 cells in the whole cell aggregate. The 106 centers (105 centers + the 106th center), and the coordinates of the vertices accompanying the four-center lists completely define the initial structure of the cell aggregate.

Appendix D. Delicately curved faces of polyhedral cells have the least surface area

The vertex dynamics in the present paper assumes that edges between vertices are straight. However, the space-filling arrangement of cells that have the least surface area is known to have delicately curved regular and irregular faces (Weaire and Phelan, 1996). For example, in comparison with the orthic tetrakaidecahedron (Fig. 3a), the Kelvin tetrakaidecahedron with curved hexagonal faces reduces the surface area per cell by about 0.2%. Thus, strictly speaking, the polygonal faces should not be flat in our simulation under boundary surface area minimization. That we do not find any deviation from flat faces in Fig. 6, is a limitation of our model at present.

References

- Beysens, D.A., Forgacs, G., Glazier, J.A., 2000. Cell sorting is analogous to phase ordering in fluids. *Proc. Natl Acad. Sci. USA* 97, 9467–9471.
- Bodenstein, L., 1986. A dynamic simulation model of tissue growth and cell patterning. *Cell Differ.* 19, 19–33.
- Bretschneider, T., Vasiev, B., Weijer, C.J., 1999. A model for *Dictyostelium* slug movement. *J. Theor. Biol.* 199, 125–136.
- Brodland, G.W., Chen, H.H., 2000a. The mechanics of heterotypic cell aggregates: insights from computer simulations. *ASME J. Biomech. Eng.* 122, 402–407.
- Brodland, G.W., Chen, H.H., 2000b. The mechanics of cell sorting and envelopment. *J. Biomech.* 33, 845–851.
- Chen, H.H., Brodland, G.W., 2000. Cell-level finite element studies of viscous cells in planar aggregates. *ASME J. Biomech. Eng.* 122, 394–401.
- Clem, C.J., Konig, D., Rigaut, J.P., 1997. A three-dimensional dynamic simulation model of epithelial tissue renewal. *Anal. Quant. Cytol. Histol.* 19, 174–184.
- Discher, D.E., Boal, D.H., Boey, S.K., 1998. Simulations of the erythrocyte cytoskeleton at large deformation. II. Micropipette aspiration. *Biophys. J.* 75, 1584–1597.
- Dormer, K.J., 1980. *Fundamental Tissue Geometry for Biologists*. Cambridge University Press, London.

- Drasdo, D., Forgacs, G., 2000. Modeling the interplay of generic and genetic mechanisms in cleavage, blastulation, and gastrulation. *Dev. Dyn.* 219, 182–191.
- Dubertret, B., Rivier, N., 1997. The renewal of the epidermis: a topological mechanism. *Biophys. J.* 73, 38–44.
- Dubertret, B., Rivier, N., 2000. Geometrical models of the renewal of the epidermis. *C. R. Acad. Sci. III* 323, 49–56.
- Forgacs, G., Foty, R.A., Shafrit, Y., Steinberg, M.S., 1998. Viscoelastic properties of living embryonic tissues: a quantitative study. *Biophys. J.* 74, 2227–2234.
- Foty, R.A., Forgacs, G., Pflieger, C.M., Steinberg, M.S., 1995. Liquid properties of embryonic tissues: measurement of interfacial tensions. *Phys. Rev. Lett.* 72, 2298–2301.
- Foty, R.A., Pflieger, C.M., Forgacs, G., Steinberg, M.S., 1996. Surface tensions of embryonic tissues predict their mutual envelopment behavior. *Development* 122, 1611–1620.
- Fuchizaki, K., Kusaba, T., Kawasaki, K., 1995. Computer modelling of three-dimensional cellular pattern growth. *Philos. Mag. B* 71, 333–357.
- Fung, Y.C., 1981. *Biomechanics*. Springer, New York.
- Glazier, J.A., Graner, F., 1993. Simulation of the differential adhesion driven rearrangement of biological cells. *Phys. Rev. E* 47, 2128–2154.
- Graner, F., Glazier, J.A., 1992. Simulation of biological cell sorting using a two-dimensional extended Potts model. *Phys. Rev. Lett.* 69, 2013–2016.
- Graner, F.A., Sawada, Y., 1993. Can surface adhesion drive cell rearrangement? Part II: a geometrical model. *J. Theor. Biol.* 164, 477–506.
- Honda, H., 1978. Description of cellular patterns by Dirichlet domains: the two-dimensional case. *J. Theor. Biol.* 72, 523–543.
- Honda, H., 1983. Geometrical models for cells in tissues. *Intern. Rev. Cytol.* 81, 191–248.
- Honda, H., Eguchi, G., 1980. How much does the cell boundary contract in a monolayered cell sheet? *J. Theor. Biol.* 84, 575–588.
- Honda, H., Oshibe, S., 1984. A computer simulation of cell stacking for even thickness in mammalian epidermis. *J. Theor. Biol.* 111, 625–633.
- Honda, H., Morita, T., Tanabe, A., 1979. Establishment of epidermal cell columns in mammalian skin: computer simulation. *J. Theor. Biol.* 81, 745–759.
- Honda, H., Ogita, Y., Higuchi, S., Kani, K., 1982. Cell movements in a living mammalian tissue: long-term observation of individual cells in wounded corneal endothelia of cats. *J. Morphol.* 174, 25–39.
- Honda, H., Dan-Sohkawa, M., Watanabe, K., 1983. Geometrical analysis of cells becoming organized into a tensile sheet, the blastular wall, in the starfish. *Differentiation* 25, 16–22.
- Honda, H., Yamanaka, H., Dan-Sohkawa, M., 1984. A computer simulation of geometrical configurations during cell division. *J. Theor. Biol.* 106, 423–435.
- Honda, H., Yamanaka, H., Eguchi, G., 1986. Transformation of a polygonal cellular pattern during sexual maturation of the avian oviduct epithelium. *J. Embryol. Exp. Morphol.* 98, 1–19.
- Honda, H., Tanemura, M., Yoshida, A., 1990. Estimation of neuroblast number in insect neurogenesis using the lateral inhibition hypothesis of cell differentiation. *Development* 110, 1349–1352.
- Honda, H., Tanemura, M., Imayama, S., 1996. Spontaneous architectural organization of mammalian epidermis from random cell packing. *J. Invest. Dermatol.* 106, 312–315.
- Honda, H., Tanemura, M., Yoshida, A., 2000. Differentiation of wing epidermal scale cells in a butterfly under the lateral inhibition model—appearance of large cells in a polygonal pattern. *Acta Biotheor.* 48, 121–136.
- Kawasaki, K., Nagai, T., Nakashima, K., 1989. Vertex models for two-dimensional grain growth. *Philos. Mag. B* 60, 399–421.
- Lang, F., Busch, G.L., Ritter, M., Völkl, H., Waldegger, S., Gulbins, E., Häussinger, D., 1998. Functional significance of cell volume regulatory mechanisms. *Physiol. Rev.* 78, 247–306.
- Lewis, F.T., 1923. The typical shape of polyhedral cells in vegetable parenchyma and the restoration of that shape following cell division. *Proc. Am. Acad. Arts Sci.* 58, 537–552.
- Lewis, F.T., 1928. The shape of cork cells: a simple demonstration that they are terakaidecahedral. *Science* 68, 625–626.
- Lewis, F.T., 1931. A comparison between the mosaic of polygons in a film of artificial emulsion and the pattern of simple epithelium in surface view (cucumber epidermis and human amnion). *Anat. Rec.* 50, 235–265.
- Lewis, F.T., 1943. The geometry of growth and cell division in epithelial mosaic. *Am. J. Bot.* 30, 766–776.
- Marée, A.F., Hogeweg, P., 2001. How amoeboids self-organize into a fruiting body: multicellular coordination in *Dictyostelium discoideum*. *Proc. Natl Acad. Sci. USA* 98, 3879–3883.
- Marée, A.F., Hogeweg, P., 2002. Modelling *Dictyostelium discoideum* morphogenesis: the culmination. *Bull. Math. Biol.* 64, 327–353.
- Meineke, F.A., Potten, C.S., Loeffler, M., 2001. Cell migration and organization in the intestinal crypt using a lattice-free model. *Cell Prolif.* 34, 253–266.
- Mombach, J.C., Glazier, J.A., Raphael, R.C., Zajac, M., 1995. Quantitative comparison between differential adhesion models and cell sorting in the presence and absence of fluctuations. *Phys. Rev. Lett.* 75, 2244–2247.
- Mombach, J.C.M., De Almeida, R.M.C., Thomas, G.L., Upadhyaya, A., Glazier, J.A., 2001. Bursts and cavity formation in *Hydra* cells aggregates: experiments and simulations. *Physica A* 297, 495–508.
- Nagai, T., Honda, H., 2001. A dynamic cell model for the formation of epithelial tissue. *Philos. Mag. B* 81, 699–719.
- Nagai, T., Kawasaki, K., Nakamura, K., 1988. Vertex dynamics of two-dimensional cellular patterns. *J. Phys. Soc. Jpn.* 57, 2221–2224.
- Nagai, T., Ohta, S., Kawasaki, K., Okuzono, T., 1990. Computer simulation of cellular pattern growth in two and three dimensions. *Phase Transitions* 28, 177–211.
- Ohno, Y., Isoda, K., 1977. *Suuchi Keisan Handobukku*. Ohmu, Tokyo (in Japanese).
- Okada, Y., 1997. Volume expansion-sensing outward-rectifier Cl^- channel: fresh start to the molecular identity and volume sensor. *Am. J. Physiol.* 273, C755–C789.
- Owaribe, K., Masuda, H., 1982. Isolation and characterization of circumferential microfilament bundles from retinal pigmented epithelial cells. *J. Cell Biol.* 95, 310–315.
- Owaribe, K., Kodama, R., Eguchi, G., 1981. Demonstration of contractility of circumferential actin bundles and its morphogenetic significance in pigmented epithelium in vitro and in vivo. *J. Cell Biol.* 90, 507–514.
- Palsson, E., 2001. A three-dimensional model of cell movement in multicellular systems. *Future Generation Comput. System* 17, 835–852.
- Palsson, E., Othmer, H.G., 2000. A model for individual and collective cell movement in *Dictyostelium discoideum*. *Proc. Natl Acad. Sci. USA* 97, 10448–10453.
- Phillips, H.M., Davis, G.S., 1978. Liquid-tissue mechanics in amphibian gastrulation: germ-layer assembly in *Rana pipiens*. *Am. Zool.* 18, 81–93.
- Phillips, H.M., Steinberg, M.S., 1978. Embryonic tissues as elasticoviscous liquids. I. Rapid and slow shape changes in centrifuged cell aggregates. *J. Cell Sci.* 30, 1–20.
- Phillips, H.M., Steinberg, M.S., Lipton, B.H., 1977. Embryonic tissues as elasticoviscous liquids. II. Direct evidence for cell slippage in centrifuged aggregates. *Dev. Biol.* 59, 124–134.
- Rivier, N., Dubertret, B., 1995. Why does skin stay smooth? The dynamics of tissues in statistical equilibrium. *Philos. Mag. B* 72, 311–322.

- Rivier, N., Dubertret, B., 1998. The renewal and statistical equilibrium of the epidermis: biomechanics of tissues. In: Inan, E., Markov, K.Z. (Eds.), *Continuum Models and Discrete Systems*. World Scientific, New Jersey, USA, pp. 318–320.
- Savill, N., Hogeweg, P., 1997. Modelling morphogenesis: from single cells to crawling slugs. *J. Theor. Biol.* 184, 229–235.
- Stein, M.B., Gordon, R., 1982. Epithelia as bubble rafts: a new method for analysis of cell shape and intercellular adhesion in embryonic and other epithelia. *J. Theor. Biol.* 97, 625–639.
- Tanemura, M., 1988. Random packing and random tessellation in relation to the dimension of space. *J. Microsc.* 151, 247–255.
- Tanemura, M., 1992. Models and simulations of random structure of particles. *Acta Stereol.* 11 (Suppl. I), 41–52.
- Tanemura, M., Ogawa, T., Ogita, N., 1983. A new algorithm for three-dimensional Voronoi tessellation. *J. Comput. Phys.* 51, 191–207.
- Tanemura, M., Honda, H., Yoshida, A., 1991. Distribution of differentiated cells in a cell sheet under the lateral inhibition rule of differentiation. *J. Theor. Biol.* 153, 287–300.
- Upadhyaya, A., Rieu, J.-P., Glazier, J.A., Sawada, Y., 2001. Anomalous diffusion and non-Gaussian velocity distribution of *Hydra* cells in cellular aggregates. *Physica A* 293, 549–558.
- Weliky, M., Oster, G., 1990. The mechanical basis of cell rearrangement. I. Epithelial morphogenesis during *Fundulus* epiboly. *Development* 109, 373–386.
- Weliky, M., Minsuk, S., Keller, R., Oster, G., 1991. Notochord morphogenesis in *Xenopus laevis*: simulation of cell behavior underlying tissue convergence and extension. *Development* 113, 1231–1244.
- Weaire, D., Kermode, J.P., 1983. Computer simulation of a two-dimensional soap froth. I. Method and motivation. *Philos. Mag. B* 48, 245–259.
- Weaire, D., Kermode, J.P., 1984. Computer simulation of a two-dimensional soap froth. II. Analysis of results. *Philos. Mag. B* 50, 379–395.
- Weaire, D., Phelan, R., 1996. A counter-example to Kelvin's conjecture on minimal surfaces. In: Weaire, D. (Ed.), *The Kelvin Problem*. Taylor and Francis, London, pp. 47–51.
- Weaire, D., Rivier, N., 1984. Soap, cells and statistics—random patterns in two-dimensions. *Contemp. Phys.* 25, 59–99.
- Weaire, D., Bolton, F., Molho, P., Glazier, J.A., 1991. Investigation of an elementary model for magnetic froth. *J. Phys.: Condens. Matter* 3, 2101–2114.
- Wejchert, J., Weaire, D., Kermode, J.P., 1986. Monte Carlo simulation of the evolution of a two-dimensional soap froth. *Philos. Mag. B* 53, 15–24.
- Wooten, F., 2002. Structure, odd lines and topological entropy of disorder of amorphous silicon. *Acta Crystallogr. A* 58, 346–351.
- Wooten, F., Winer, K., Weaire, D., 1985. Computer generation of structural models of amorphous Si and Ge. *Phys. Rev. Lett.* 54, 1392–1395.